Proceedings of Turbo Expo 2003
ASME TURBO EXPO 2003: Power for Land, Sea, and Air
June 16–19, 2003, Atlanta, Georgia, U.S.A.

GT2003-38839

MEASUREMENTS AND PREDICTIONS OF HEAT TRANSFER ON ROTOR BLADES IN A TRANSONIC TURBINE CASCADE

Paul W. Giel
QSS Group, Inc.
NASA Glenn Research Center
Cleveland, Ohio 44135 USA
Email: Paul.W.Giel@grc.nasa.gov

Robert J. Boyle
NASA Glenn Research Center
Cleveland, Ohio, 44135 USA
Email: Robert.J.Boyle@grc.nasa.gov

Ronald S. Bunker
General Electric Co.
Global Research Center
Schenectady, New York, 12301 USA
Email: bunker@crd.ge.com

ABSTRACT

Detailed heat transfer measurements and predictions are given for a power generation turbine rotor with 127 deg of nominal turning and an axial chord of 130 mm. Data were obtained for a set of four exit Reynolds numbers comprised of the facility maximum point of 2.50×10^6, as well as conditions which represent 50%, 25%, and 15% of this maximum condition. Three ideal exit pressure ratios were examined including the design point of 1.443, as well as conditions which represent −25% and +20% of the design value. Three inlet flow angles were examined including the design point and ±5 deg off-design angles. Measurements were made in a linear cascade with highly three-dimensional blade passage flows that resulted from the high flow turning and thick inlet boundary layers. Inlet turbulence was generated with a blown square bar grid. The purpose of the work is the extension of three-dimensional predictive modeling capability for airfoil external heat transfer to engine specific conditions including blade shape, Reynolds numbers, and Mach numbers. Data were obtained by a steady-state technique using a thin-foil heater wrapped around a low thermal conductivity blade. Surface temperatures were measured using calibrated liquid crystals. The results show the effects of strong secondary vortical flows, laminar-to-turbulent transition, and also show good detail in the stagnation region.

NOMENCLATURE

A	heater area [m^2]
C_x	blade axial chord [mm]
d	leading edge diameter [mm]
Fr	Frossling number, $Fr = Nu \cdot (d/C_x)/\sqrt{Re_{d,in}}$
h	heat transfer coefficient [$W/m^2 \cdot K$]
K	pressure gradient parameter, $K = (\mu/\rho U^2)(dU/ds)$
k	thermal conductivity [W/m·K]
k^+	normalized roughness height
M	Mach number
Nu	Nusselt number, $Nu = h \cdot C_x/k$
P	pressure [Pa]
Pr	Prandtl number
PR	exit pressure ratio, $PR = P'_{in}/P_{ex}$
q''	heat flux [W/m^2]
r	recovery factor, $r = Pr^{1/3}$
Re_{ex}	Reynolds number, $Re_{ex} = \rho U_{ex} C_x/\mu$
s	blade surface coordinate, normalized by C_x
T	temperature [K]
Tu	turbulence intensity
U	total velocity [m/s]
y^+	equivalent normal distance
z	spanwise coordinate, normalized by blade span
α	relative incidence angle [degrees]
δ	99% boundary layer thickness [mm]
Λ_x	longitudinal integral turbulence length scale [mm]
μ	dynamic viscosity [kg/s·m]
μ_t	turbulent eddy viscosity [kg/s·m]
ρ	density [kg/m^3]

Subscripts

$_{aw}$	adiabatic wall temperature
$_{fs}$	freestream inviscid value
$_{lc}$	liquid crystal
$_{ex}$	exit isentropic value
$_{in}$	inlet freestream value
$_{is}$	isentropic value

Superscripts

$'$	total conditions

INTRODUCTION

Turbine blade aerodynamics is generally given a high degree of analysis prior to commitment for fabrication. This attention to detail is carried through to the manufacturing specifications and quality inspections in the form of dimensional accuracies demanded of both the airfoils and the rotor disks. While a substantial amount of data exists concerning the effects of blade incidence angle, Reynolds number, and pressure ratio (loading) on aerodynamics, less information is available on the associated airfoil heat transfer distributions for off-design conditions. Computational Fluid Dynamics (CFD) is increasingly being relied upon in the design and analysis of gas turbine components. The need to predict heat transfer along with aerodynamics during the design of turbine blades greatly complicates these analyses. Thus, the heat transfer predictive capability of CFD currently lags that of aerodynamics. Heat transfer data is therefore needed both to assess the effects of various flow parameters and to improve CFD analyses so that these effects can be accurately predicted.

Arts et al., (1998) studied incidence, Reynolds number, and exit Mach number effects on heat transfer, but with midspan thermocouples only. Incidence was varied over a range of -14 deg to $+11$ deg. Camci and Arts (1991) also examined incidence effects on a film-cooled heat transfer test blade, but again only at midspan. The three-dimensional nature of the flow and heat transfer indicates that a full-blade understanding is needed, not just a two-dimensional understanding at midspan. Previous studies have shown that rotor geometries in linear cascades provide good midspan data as compared to their rotating equivalents. See, for example, Baughn et al. (1995) or Guenette et al. (1989). Also, Graziani et al. (1980) studied the effects of thick and thin endwall boundary layers on rotor heat transfer in a low speed linear cascade. Blair (1994) measured heat transfer in a low speed facility on a rotating blade that had the same midspan section as the blade of Graziani et al. (1980). Similar three-dimensional heat transfer patterns were observed at and below midspan of those two tests, validating the use of linear cascades for these types of heat transfer studies. Dunn et al. (1994) measured rotor heat transfer at discrete chordwise and spanwise locations in a shock tube facility at engine-typical gas-to-wall temperature ratios and Mach numbers. These measurements were on engine-size hardware using heat flux gauges. Consequently, the resolution was less than for the large scale facility measurements.

Detailed heat transfer data at conditions approximating those in actual engines are needed to assess flow parameter effects and to verify CFD predictive analyses over a wide range of operating conditions. Variations in flow parameters often have an impact on secondary flows and thus on the three-dimensional nature of the heat transfer distribution. Data is therefore needed all over the blade surface, not just at midspan.

Parameter	Value
axial chord	129.8 mm (5.110 in.)
pitch	130.0 mm (5.119 in.)
span	152.4 mm (6.000 in.)
d, leading edge	18.4 mm (0.726 in.)
turbulence grid	25.4 mm square bar
blade passages	11

(d = 2 × minimum radius of curvature)

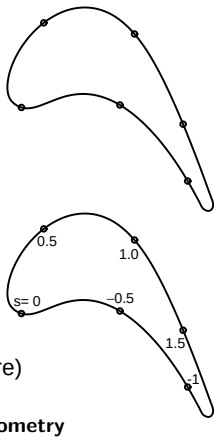

Figure 1. Test Blade Geometry

The blade geometry of the present study is representative of a first stage turbine blade for a new GE heavy frame power turbine machine design. The present design is a heavily loaded blade using highly effective internal cooling with limited film cooling. The blade aerodynamic section is relatively thick in conjunction with a low solidity blade row design, and contains a large leading edge diameter. Knowledge of the external convective heat transfer distribution is desired for both validation and for the improvement of predictive methods. The turbine blade is for a machine operating in the 1370°C (2500°F) class. The full power design point isentropic pressure ratio of the current blade section is 1.443. The inlet Mach number is 0.399 and the exit isentropic Mach number is 0.743. The inlet angle of attack is 59.1 deg while the exit angle is 67.9 deg, producing an aggressive total turning of 127 deg. The airfoil Reynolds number is 2.68×10^6 based upon axial chord length and exit conditions. The test facility inlet plenum pressure cannot exceed 162 kPa (23.5 psia), which limits the exit Reynolds number to 2.50×10^6. For the purposes of this report therefore, this later value will be referred to as the design Reynolds number. The blade geometry is shown in Fig. 1 along with geometric details. Surface distance coordinates are also shown on the blade.

Tests have been conducted covering a range of blade pressure ratios from -25% to $+20\%$ of the design nominal condition, spanning the full spectrum from well subsonic ($M_{ex,is} = 0.33$) to transonic ($M_{ex,is} = 0.92$). Reynolds numbers as low as 15% of the design point allow the evaluation of heat transfer distributions over conditions from turning crank to first fire to full power. In addition, inlet attack angle variations of $+5$ deg and -5 deg have been investigated. All of these test conditions serve to map out a

large performance space with significant alterations in pressure and heat transfer distributions, and consequent challenges for numerical predictive techniques.

The set of data produced in this study serves as a test of CFD predictive capability for an actual airfoil design space. The primary objective of this research is the continued extension of three-dimensional predictive modeling techniques for airfoil external heat transfer through the acquisition of full-surface blade data. Previous blade heat transfer studies in this facility include Giel et al. (1999) and Giel et al. (2000). The airfoil shape of the current study is distinctly different than those previously tested in the same facility, thus providing a new CFD test case for previously validated predictive techniques. The CFD comparisons are challenged further by the wider variations of incidence angle, pressure ratio, and Reynolds number. The CFD predictions, when compared to the measurements, point out areas where modeling improvements are needed. Liquid crystal surface temperature measurement techniques are capable of obtaining detailed data over an entire surface and were therefore chosen for the present study.

DESCRIPTION OF FACILITY

Cascade Description

The NASA Glenn Research Center Transonic Turbine Blade Cascade provides heat transfer and aerodynamic data to verify CFD analyses. The facility can and has been used to test over wide, independent ranges of Reynolds number and Mach number. High pressure, ambient temperature air can be throttled to an inlet pressure that can be varied from the exit pressure to 162 kPa (23.5 psia). The exhaust pressure can be varied independently from the inlet pressure down to 13.8 kPa (2.0 psia). The facility operates in a continuous mode with mass flow rates for the current study ranging from 3.2 kg/s (7.1 lb_m/s) to 26.3 kg/s (58.0 lb_m/s). A two-dimensional view of the facility is shown in Fig. 2. Heat transfer measurements were made on the sixth of twelve blades counting from left to right. The pressure measurement blades were the fifth and sixth. The flowpath width of the portion of the facility shown in Fig. 2 is uniform and matches the blade span.

While the blade and cascade geometries are two-dimensional, the blade passage flows are highly three-dimensional due to the aggressive turning, the thick boundary layers developed on the long cascade inlet, and the low aspect ratio blades ($span/C_x = 1.17$). The thickness of each endwall boundary layer varied from 28% to 37% of the half-span depending on the inlet Reynolds number, as estimated from measurements approximately one axial chord

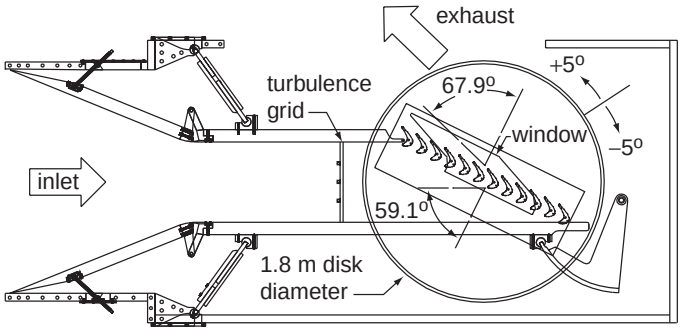

Figure 2. Transonic Turbine Blade Cascade Facility

upstream of the blade row. The thick boundary layers and high flow turning resulted in spanwise flow variations as large as those seen in rotating turbines. See, for example, Joslyn and Dring (1992) or Thulin et al. (1982). These variations result from secondary flows, and accurately predicting them is a significant test of a three-dimensional analysis.

Inlet turbulence was produced using a square bar, bidirectional grid upstream of the blade row. The grid was made of 25.4 mm (1 inch) square hollow bars with 75 uniformly spaced 3.2 mm (1/8 in.) diameter holes blowing air in the upstream direction. One bar extended between the inlet boards at midspan and three bars spaced six bar dimensions apart were placed spanwise as shown in Fig. 2. The total mass flow from the grid was 0.68 kg/s (1.5 lb_m/s) for all cases, corresponding to 2.6% of the cascade mass flow at the design exit Reynolds number. The open area of the grid was 74% and it was located 1.10 m (43 in.) upstream of the heat transfer measurement blade. It was positioned normal to the inlet flow as shown in Fig. 2. An aerodynamic probe measurement slot was located an axial distance of 127 mm in front of the cascade face. Results of the inlet turbulence measurements can be found in a previous study by Giel et al. (1999). The blades of the current study have the same pitch and are located at the same distance from the grid as those of the previous study. The inlet turbulence level measured there was approximately 9% at an inlet Mach number of 0.39. The longitudinal, integral turbulence length scale was measured to be $\Lambda_x = 26$ mm. Pitchwise and spanwise surveys of mean velocity, Tu, and length scale were made in the probe slot over several blade passages.

Boyle et al. (2002) found that there could be a substantial increase in apparent turbulence intensity at the design inlet Mach number when a correction is made to account for Knudsen number effects on small diameter wires. The inlet turbulence intensity was measured as 9%, but the Knudsen number effect was not accounted for. Accounting for the Knudsen number effect increased Tu_{in} from 9% to 13%.

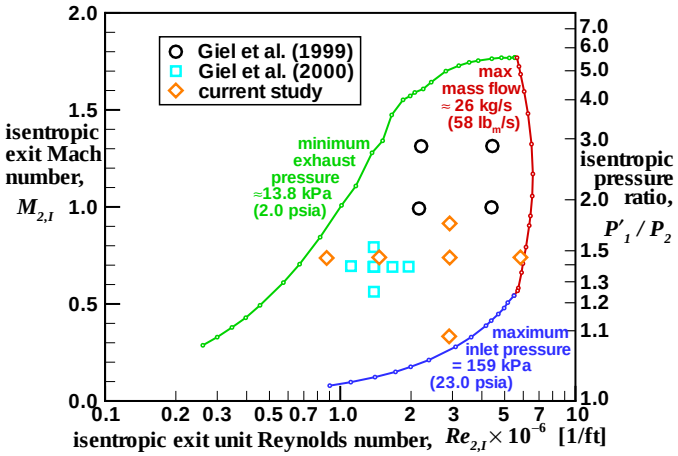

Figure 3. Facility Operating Parameters

Additional measurements showed that as the Mach number decreased, the uncorrected turbulence level increased. The corrected turbulence level of 13% was found to be nearly the same for all inlet Mach numbers.

Figure 2 shows the test section mounted on a large rotatable disk. The disk can be rotated +15 deg to −30 deg to accommodate blades with different inlet flow angles as well as to vary the incidence angle. Upstream inlet boards were used, but the facility uses no exit tailboards. Endwall static pressure measurements and other flow field aerodynamic probe measurements all showed excellent periodicity in at least the center three blade passages (see Giel et al., 1996). The flow conditions of two previous blade heat transfer studies are shown in Fig. 3 along with those of the current study. The conditions are shown as unit exit Reynolds number *vs.* exit isentropic Mach number or pressure ratio. The operating envelope of the facility is also shown in the figure with limits imposed by minimum exhaust pressure, maximum mass flow, and maximum inlet pressure.

Pressure Measurement Blade Description

The two blades forming passage 5 were instrumented for pressure measurements. Blade 5 had 18 static pressure taps at 10% span and 20 more at 25% span. Blade 6 had 38 taps at midspan. The tap diameters were 0.5 mm (0.020 in.).

Heat Transfer Measurement Blade Description

The blade in position 6 was fabricated from low conductivity foam ($k = 0.2$ W/m · K) for heat transfer measurements. The undersized foam core was placed in a mold and gelcoat epoxy was cast around it. The outer epoxy shape was itself undersized by 152 μm (0.006 in.) to accommodate a 25 μm (0.001 in.) Inconel thin foil heater and a 127 μm (0.005 in.) double-faced adhesive layer. The single sheet heater covered the entire blade except on the trailing edge circle. Two thin-film thermocouples were glued to the heater sheet at $z = 0.25$, one on the pressure surface at $s = -0.21$ and one on the suction surface at $s = 1.81$. These were used for overheat control and for liquid crystal temperature verification. Flat black paint was sprayed over the outer surface and a 25×25 mm (1×1 in.) grid of white dots was painted on for location reference. Finally, chiral nematic, micro-encapsulated liquid crystals were sprayed onto the outer heater surface. A temperature calibration plate, instrumented with a thermocouple, and a roughness measurement plate were sprayed at the same time. The liquid crystal yellow-line temperature was calibrated with the calibration plate and verified during data acquisition with the two blade surface-mounted thermocouples. Both ends of the blade were made of 12.7 mm (0.50 in.) thick nickel-plated copper, cut out in the shape of the blade, and were used as buss bars to supply DC electrical power to the heater. The heater foil extended over the copper ends and was tack welded to them. Hollow studs extended from the copper, through the acrylic windows, and were used for mounting and for electrical connections. They were also connected through vacuum tubing to the exhaust section of the facility to approximately equalize the pressure inside and outside of the blade, preventing damage to the surface when the test section pressure was changed. Both endwalls were 63.5 mm (2.50 in.) thick clear acrylic for optical access. An outline of the window is shown in Fig. 2.

A profilometer was used to measure several 5-mm traces on the roughness measurement plate after the liquid crystals were applied. The arithmetic mean roughness was 3.7 μm and the r.m.s. roughness was 4.7 μm. The average peak-to-peak distance was 62 μm. Estimates of the equivalent roughness height ranged between 3.7 μm and 23 μm. The maximum equivalent height corresponds to an estimated maximum k^+ of 13.6. Blade surface heat transfer could have been influenced by roughness at the higher Reynolds numbers. Even if the average roughness value was the same as that of an in-service blade, the roughness distribution is likely to be different.

MEASUREMENT TECHNIQUES

Blade Static Pressure Measurements

Surface static pressures were measured independently from the heat transfer measurements using a separate blade set. The two blades forming passage 5 were instrumented with 76 static pressure taps. The pressure taps were scanned at a rate of once per second with an electronically

scanned measurement system. Fifteen scans were averaged. The inlet total pressure was measured as the average of three midspan Kiel probes upstream of passages 4, 7, and 8. The probes were located an axial distance of 127 mm (5.0 in.) ahead of the cascade face. More details of the blade static pressure measurement techniques are given by Giel et al. (1996).

Heat Transfer Measurements

The selections of liquid crystal yellow line temperatures and color band widths were made subject to several constraints. The crystal temperature was chosen to be as high as possible to minimize uncertainty without exceeding the 80°C (175°F) material limit of the double-faced adhesive. This limit was approached in regions of minimum heat transfer when the heater power was increased to make measurements in regions of maximum heat transfer. A crystal temperature 16°C (29°F) above the inlet total temperature typically met both criteria. The measured yellow line crystal temperature was 37.3°C (99.1°F) and the inlet air varied between 5.1°C (41.2°F) and 22.3°C (72.2°F). Narrower bandwidth crystals provide better resolution in regions of very low gradients but the yellow line could become too thin to be clearly visible in high gradient regions. Crystals with full color bandwidths of ±2°C were found to be a good compromise for the current measurements.

The following procedure was used to obtain the heat transfer data: Flow conditions were established and the heater power was increased until the first yellow isotherm was visible. When steady state conditions were achieved, typically within 10 minutes, data recording of voltage, current, and flow conditions was initiated. The blade surface was simultaneously photographed with four 35 mm still cameras using color slide film. Each camera photographed a subset of the blade surface, with some overlap between views. Moffat (1990) showed that micro-encapsulated crystals are less sensitive to illuminating and viewing angles than non-encapsulated crystals. High speed photographic strobes were used to prevent radiative heating of the liquid crystals. The strobes were mounted as close as possible to the camera lens to minimize differences between viewing and illumination angles. No differences in isotherm location were detected between overlapping photographs. Heater power was then increased to move the isotherms and the process was repeated until the entire blade surface was mapped. 24 power levels were typically used for each flow condition.

The following procedure was used to reduce the heat transfer data. The photographic slide images were projected onto paper and the reference dot pattern and the isotherms were sketched. The slide image dot pattern was aligned for subsequent isotherms. Separate sketches were made for each camera view. These composite isotherm sketches were then digitized, with between 4000 to 8000 digitized points for each flow condition. A grid having five times the resolution of the blade dot pattern painted was laid over the blades and photographed. Every fifth point on the grid photograph was aligned with the dots in the data photographs. The finer resolution coordinates were then used to interpolate each digitized point to (s, z) unwrapped blade coordinates. This procedure corrected for distortions due to blade curvature and viewing angles.

The local surface heat flux, q'', was determined from the heater voltage, V [volts], and current, I [amps], then corrected for radiative heat loss:

$$q'' = \frac{V \cdot I}{A} - \epsilon\sigma(T_{lc}^4 - T_{aw}^4)$$

With the emissivity, ϵ, assumed to be 0.98, radiative losses were at most 8.8% of the net heat flux at the lowest Reynolds number and declined rapidly with increasing Reynolds number to a local maximum of only 1.3% at the highest Reynolds number. Here, σ is the Stefan-Boltzmann constant. The heat transfer coefficient and the Nusselt number were defined as follows:

$$h = \frac{q''}{(T_{lc} - T_{aw})} \quad \text{and} \quad Nu = \frac{h \cdot C_x}{k(T'_{in})} \tag{1}$$

The local adiabatic wall temperature, T_{aw}, is:

$$\frac{T_{aw}}{T'_{in}} = r + \frac{1 - r}{1 + 0.5(\gamma - 1)M_{is}^2}$$

with the specific heat ratio, $\gamma = 1.4$. The choice of T_{aw} as the convective driving temperature ensures that h and Nu are reasonably independent of the thermal boundary condition, specifically, independent of the particular choice of liquid crystal temperature. The inlet total temperature, T'_{in}, was determined by a mass weighted average of the main flow and the turbulence grid flow. Two additional total temperature probes were located an axial distance of 127 mm (5.0 in.) ahead of the cascade face and agreed with the mass weighted average to within the measurement uncertainty. The local adiabatic wall temperature was needed at each digitized point in order to calculate the heat transfer coefficient. This information was interpolated from CFD

calculations of blade surface static pressure which will be shown to agree well with measured values. The calculated values provided significantly better spatial resolution than was available from the experimental data. The isentropic Mach number, M_{is}, was determined from CFD calculations, and a recovery factor of $r = Pr^{1/3}$ was used everywhere. The data were triangulated for contour plotting and interpolated onto constant span lines of 15%, 25%, and 50% for line plotting.

Uncertainty Analysis

An uncertainty analysis was performed using the method of Kline and McClintock (1953). The major sources of uncertainty in Eq. 1 are the adiabatic wall temperature, $\delta T_{aw} = \pm 1.0°\text{C}$ ($\pm 1.8°\text{F}$) and the liquid crystal temperature, $\delta T_{lc} = \pm 0.5°\text{C}$ ($\pm 0.9°\text{F}$). At the temperature differences and the relatively low Mach numbers of the current study, the uncertainty in pressure measurements, the differences between measured and calculated pressures, and the interpolations are minor contributors to the overall uncertainty of T_{aw} as compared to the uncertainty in T'_{in}. The uncertainty in T_{aw} for the same reason assumes no uncertainty in the recovery factor, r, although it is not precisely known as shown by Schlichting (1979). Other less dominant sources of uncertainty such as the heater voltage and current, $\delta V/V = \delta I/I = 1\%$, and the heater length and width, $\delta L/L = 2\%$ and $\delta W/W = 1\%$, were included in the analysis. The overall uncertainty in Nu was determined to be less than 8.2% for all cases and was typically less. Because the uncertainty varied with specific conditions, maximum values for each case will be presented with the results.

CFD ANALYSIS

To illustrate where analysis improvements are needed, baseline CFD results were done using the three-dimensional Navier-Stokes analysis code, *RVC3D*, described by Chima and Yokota (1990) and by Chima (1991). C-type grids were generated using the method of Arnone et al. (1992). Further details of the computational approach are found in Giel et al. (2000). Predictions were made using a $313 \times 49 \times 65$ grid. The grid size was based on previous work, (Boyle and Giel, 1995). Even though the Reynolds number, and therefore y_1^+ varied by more than a factor of six, all comparisons were made using the same grid. A uniform blade temperature of $1.15 \times T'_{in}$ was specified. The temperature of the unheated endwall was set equal to the inlet total temperature. Midspan symmetry was assumed.

A two-layer algebraic turbulence model, described by Chima et al. (1993), was used. Transition start was specified using Mayle's (1991) model. The start of transition is a function of the local momentum thickness and turbulence intensity. The freestream turbulence level for the start of transition was calculated using the relationship given by Steelant and Dick (1999). The measurements of Boyle et al. (2002) showed that this relationship predicted the change in midpassage turbulence in a turbine vane cascade. The transition length model of Boyle and Simon (1999) was used. This model is an extension of the one by Solomon et al. (1995) to include Mach number effects.

The analysis incorporated a model to account for the effects of freestream turbulence on eddy viscosity. This model was based on the Smith and Kuethe (1966) model for the effects of turbulence in the leading edge region. The Smith and Kuethe model gives:

$$\mu_t = C_{SK}\, l\, \rho\, Tu_{in}\, U_{in}$$

Augmentation of the viscosity due to freestream turbulence effects are needed, not only in the leading edge region, but whenever the flow is laminar. Otherwise, the laminar surface heat transfer is often underpredicted. Dullenkopf and Mayle (1995) suggested that the velocity gradient is the important parameter for use in augmenting laminar heat transfer. In the leading edge region $dU/ds = a_1 U/d$. To first order $a_1 = 4$. For a variable velocity gradient, μ_t is calculated from:

$$\mu_t = C_{DM}\, C_{SK}\, l\, \rho\, Tu_{in}\, U_{fs} \sqrt{d \left(\frac{dU_{fs}}{ds}\right) \left(\frac{1}{U_{fs}}\right)}$$

The square root is used because, in the Dullenkopf and Mayle model Tu is also a function of $\sqrt{dU/ds}$. $C_{SK} = 0.00164$, Tu in percent. $C_{DM} = 0.5$. Both equations for μ_t are independent of length scale. Experiments, (Ames and Moffat (1990) and Van Fossen et al. (1995)) showed that increasing the scale of turbulence decreases heat transfer. From a computational standpoint there are disagreements in the literature. According to Dullenkopf and Mayle (1995), there is a peak in Frossling number at a specific normalized length scale. Length scales greater or less than this value result in lower Frossling numbers. Also, the equation for μ_t uses the leading edge diameter. This may not be appropriate for modeling turbulence intensity effects on the pressure surface away from the leading edge. The analyses were done assuming that Tu_{in} is 13%.

BLADE STATIC PRESSURE RESULTS

Figure 4 shows sample measured and calculated aerodynamic parameters on an unwrapped blade surface. Figure 4(a) shows calculated contours of M_{is} for the design flow case. The horizontal and vertical axes of this and all subsequent surface contour plots are scaled such that the physical blade surface distance/blade span aspect ratio is preserved. Figure 4(b) shows the corresponding comparison with data. In this case and for all other cases not presented here, the comparison with data is very good. The surface contour plot shows the strong three-dimensionality of the flow, as evidenced by the distorted suction surface contours caused by the horseshoe/passage vortices. No decelerating flow regions are seen on the suction surface until near the geometric throat at $s \approx 1.07$ where very slight deceleration occurs on the uncovered portion of the blade. Deceleration is also seen on the pressure surface just downstream of the leading edge, extending to $s \approx -0.35$. Three-dimensional distortions caused by secondary vortical flows are also seen on the pressure surface. These regions are noted because of their potential implications on flow transition and thus on heat transfer. The calculated values of M_{is} were used for heat transfer data reduction because they provided significantly better spatial resolution than was available from the experimental data.

Figure 4(c) shows the calculated pressure gradient parameter, K, at midspan for varying Reynolds numbers, all at the design pressure ratio and inlet flow angle. Again note the decelerating flow region ($K < 0$) on the pressure surface just downstream of the stagnation region. The flow then accelerates for the remainder of the pressure surface. Because K is inversely proportional to the Reynolds number, only the two lowest Reynolds number cases have pressure gradient parameters that exceed 3.5×10^{-6}. Relaminarization was predicted when K exceeded this value.

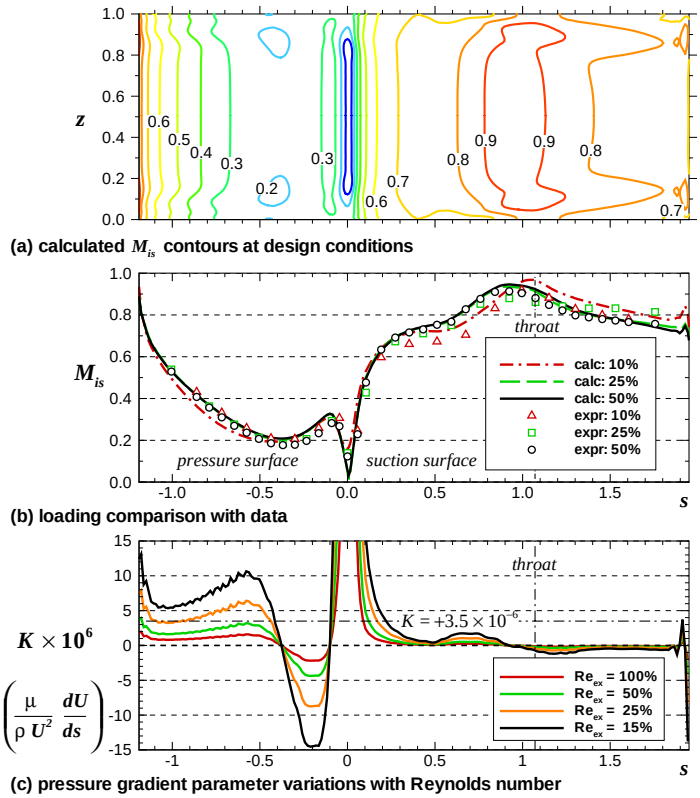

Figure 4. Measured and Calculated Blade Loadings

EXPERIMENTAL HEAT TRANSFER RESULTS

Data and CFD calculations will be presented as Nusselt number contours on the unwrapped blade surface and as line plots at 15%, 25%, and 50% span. Discussion of the experimental data will be presented first, followed by a discussion of the calculated results. Gray areas on the data contour plots indicate regions where data were not available. The copper buss bars are also evident in the data plots as regions near the endwalls where no data were available. The CFD calculations were made with a uniform temperature specified on the entire blade and did not model the buss bar thermal boundary condition. Lines showing their locations are included in the contour plots for reference. It should be noted that no midspan symmetry was assumed in presenting the experimental data; measured symmetry is typically good, but minor differences can be seen.

The measured flow conditions for the eight heat transfer cases are listed in Table 1. Data at other combinations of flow parameters were obtained but will not be presented here. The first case to be presented will be the baseline case, obtained at the design flow conditions. Subsequent cases are grouped to examine the effects of Reynolds number pressure ratio, and incidence angle. Variations in Reynolds number of 50%, 25%, and 15% (Cases 2–4) will be examined with the pressure ratio and the incidence angle held at their design values. Variations in pressure ratio of −25% and +20% (Cases 5–6) will be examined with the exit Reynolds number at 50% of its design value and the incidence angle at its design value. Pressure ratios less than the design value could not be examined at the design Reynolds number because of facility limitations (see Fig. 3). Finally, variations in incidence of ±5 deg (Cases 7–8) will be examined with the exit Reynolds number at 50% of its design value and the pressure ratio at its design value. Repeatability of Re_{ex} was within 1.2% for all cases and repeatability of PR was within 0.8%. As mentioned earlier, Nu uncertainty depended primarily on the difference between the air temperature and the liquid crystal temperature. The variations in uncertainty shown in Table 1 resulted primarily from day-to-day

Table 1. Description of Blade Heat Transfer Cases

Case	$Re_{C_x,ex}$	PR	α_{in}	$Re_{d,in}$	$\frac{\delta_{in}}{0.5 \cdot \text{span}}$	$M_{ex,is}$	max Nu uncert
1	2,488,000	1.442	0.0°	213,822	0.283	0.742	4.5%
2	1,239,000	1.435	0.0°	105,448	0.313	0.738	4.4%
3	621,900	1.446	0.0°	53,761	0.347	0.745	5.5%
4	374,700	1.445	0.0°	33,160	0.370	0.745	5.0%
5	1,237,000	1.080	0.0°	114,938	0.310	0.333	4.8%
6	1,246,000	1.735	0.0°	100,859	0.317	0.923	4.7%
7	1,238,000	1.430	−5.0°	97,150	0.317	0.734	8.2%
8	1,241,000	1.441	+5.0°	123,789	0.307	0.741	7.6%

variations in inlet air temperature. $Re_{d,in}$ is included in the table for discussion of the stagnation point heat transfer. An inlet Reynolds number based on axial chord can be calculated from this by multiplying by $C_x/d = 7.04$.

Baseline Case

Figure 5 shows the measured and predicted Nusselt number distribution at the nominal design flow condition of $Re_{ex} = 2.5 \times 10^6$, $PR = 1.443$, and $\alpha = 0$ deg. The rear portion of the pressure side data shows increasing values of Nu characteristic of turbulent flow. Figure 4(b) shows a favorable pressure gradient in this region, but Fig. 4(c) shows that the pressure gradient parameter, K, for this Reynolds number is at most 1.6×10^{-6} which is too low to expect flow relaminarization. Figure 4(b) also shows an adverse pressure gradient region downstream of $s \approx -0.1$. A local peak in Nu is seen corresponding to this region which may indicate incipient flow separation. The peak stagnation line heat transfer at $s = 0.043$ is almost indistinguishable because of the strong effects of the very rapid transition at the beginning of the suction surface. Stagnation point heat transfer values will be examined in more detail after discussing the effects of Reynolds number.

On the suction surface, for $s > 0.2$, downstream of the transition peak, Nu decreases as expected for fully turbulent flow. Midspan values of Nu decrease up to the geometric throat at $s = 1.07$. Nu increases slightly after this in the uncovered turning region. The effect of the secondary flow is seen in Fig. 5(c) as departures of the 15% and 25% data from midspan data beyond $s \approx 0.8$. Many of these effects can be attributed to the vortex structures described by Langston (1977). The passage vortex and the pressure-side leg of the horseshoe vortex approach the suction surface. Heat transfer is enhanced by the relatively cool secondary flow fluid impinging on the endwall regions of the blade suction surface.

Effects of Reynolds Number

Data were obtained at exit Reynolds numbers that were nominally 50%, 25%, and 15% of the design value. Analysis

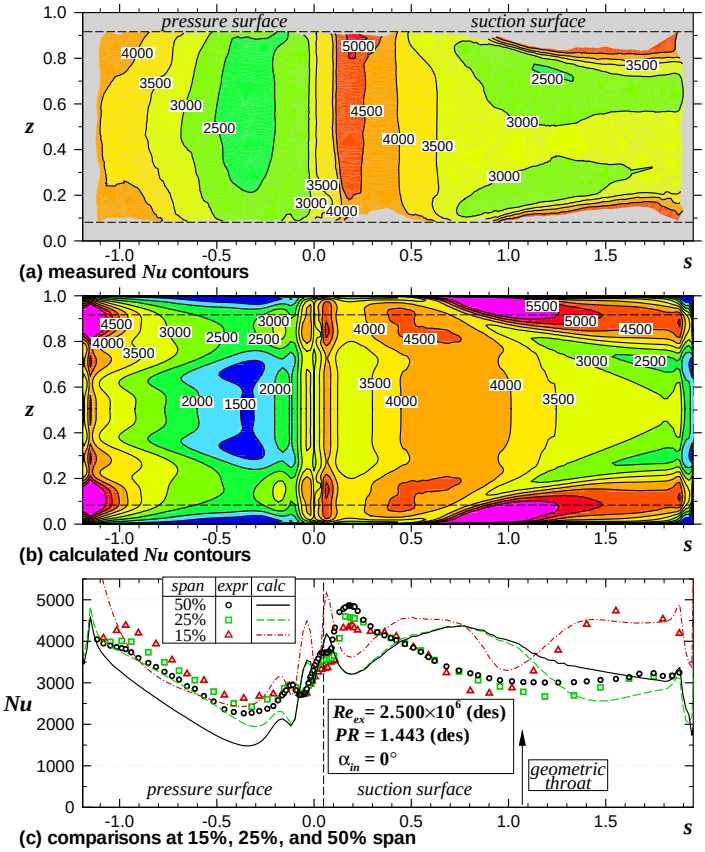

Figure 5. Heat Transfer Distributions - Case 1

of the data, particularly on the pressure surface, is aided by examination of the midspan pressure gradient parameter, K, shown in Fig. 4(c).

Figure 6 shows the data obtained at 50% of the design Reynolds number and at the design pressure ratio and incidence angle. As expected, the rear half of the pressure surface appears to again be fully turbulent. The local peak just on the pressure surface side of the stagnation region is not as severe as it was for Case 1. The stagnation line near $s = 0$ is much more evident for this case because the lower Reynolds number has caused the suction surface transition to move away from the stagnation region, appearing to begin at $s \approx 0.15$. Suction surface heat transfer rates decrease after the fully turbulent point at $s \approx 0.3$ again until reaching the throat at $s = 1.07$. Values of Nu away from midspan are then seen to increase for the remainder of the suction surface. This increase can again be attributed to the secondary flows that are evident in Fig. 6(a).

Data obtained at 25% of the design Reynolds number but again at the design pressure ratio and incidence angle are shown in Fig. 7. Recall that the maximum estimate

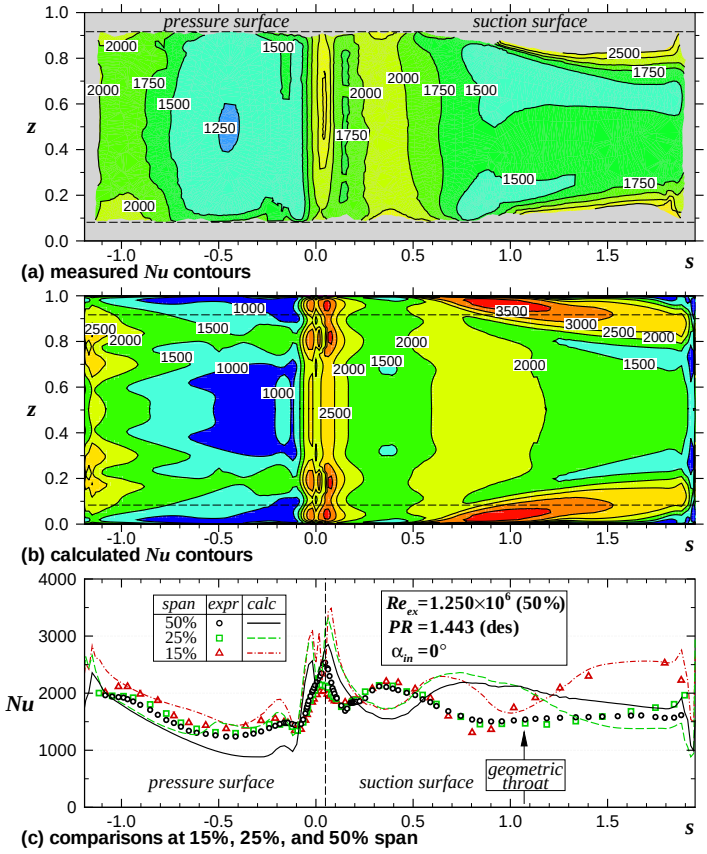

Figure 6. Heat Transfer Distributions - Case 2

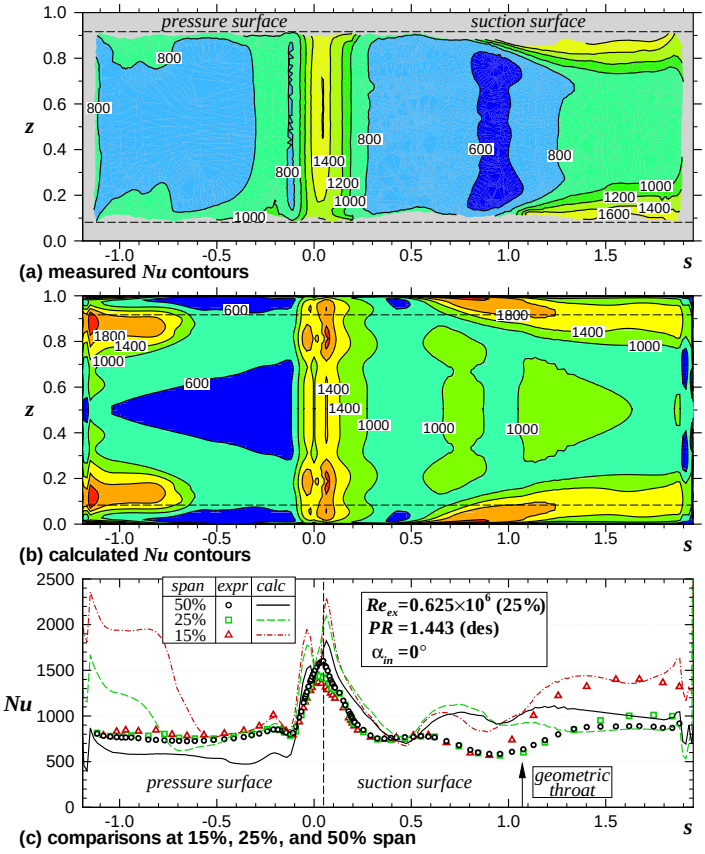

Figure 7. Heat Transfer Distributions - Case 3

of k^+ was 13.6. Because k^+ varies nearly linearly with Reynolds number, for $Re \leq 25\%$ of the maximum value, the blade is expected to be hydraulically smooth everywhere. In contrast to the first two cases, the heat transfer distribution on the pressure surface now appears to be quite uniform. This is probably due to flow relaminarization because the pressure gradient parameter shown in Fig. 4(c) significantly exceeds 3.5×10^{-6}. Relaminarization at low Reynolds number was noted in a previous study (Giel et al., 2000) with some slightly higher Reynolds number cases undergoing a second transition near the pressure surface trailing edge. This second transition does not seem to be evident in the present study. The local peak caused by the decelerating flow just downstream of the stagnation region is again less severe than for the higher Reynolds number cases. The stagnation line is very evident near $s \approx 0.04$. Despite the high inlet turbulence, the lower Reynolds number forces the suction surface transition to be delayed all the way to the point where the flow decelerates just upstream of the geometric throat. Transition then causes Nu values to increase and then level off for $s > 1.5$.

The final case showing the effects of variations in Reynolds number is shown in Fig. 8. The Reynolds number for this case is only 15% of the nominal design value. As for the 25% $Re_{Cx,ex}$ case, the heat transfer distribution on the pressure surface is quite uniform, again indicating relaminarization with no second transition. The local peak just downstream of the stagnation line is barely evident, and the stagnation line is clearly evident. Transition at midspan is delayed even further than for the 25% Re case with transition starting at the geometric throat location, $s = 1.07$. The overall contour plot in Fig. 8(a) and the 15% span data in Fig. 8(c) both show that the secondary flow effects are most significant for this case, presumably because the inlet boundary layer is 30% thicker than the design case as listed in Table 1.

The liquid crystal measurement technique is very helpful in obtaining full-surface contour plots. The data can be interpolated to obtain spatially detailed data for line plots through a subdomain as was done with the 15%, 25%, and 50% span data above. These line plots are very useful in comparing results at different flow conditions as is done

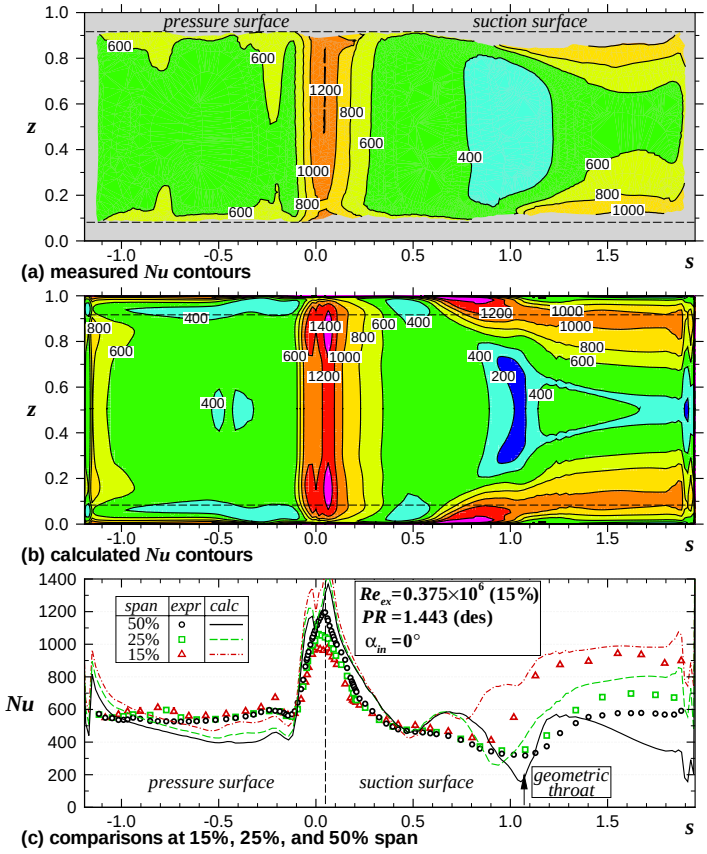

Figure 8. Heat Transfer Distributions - Case 4

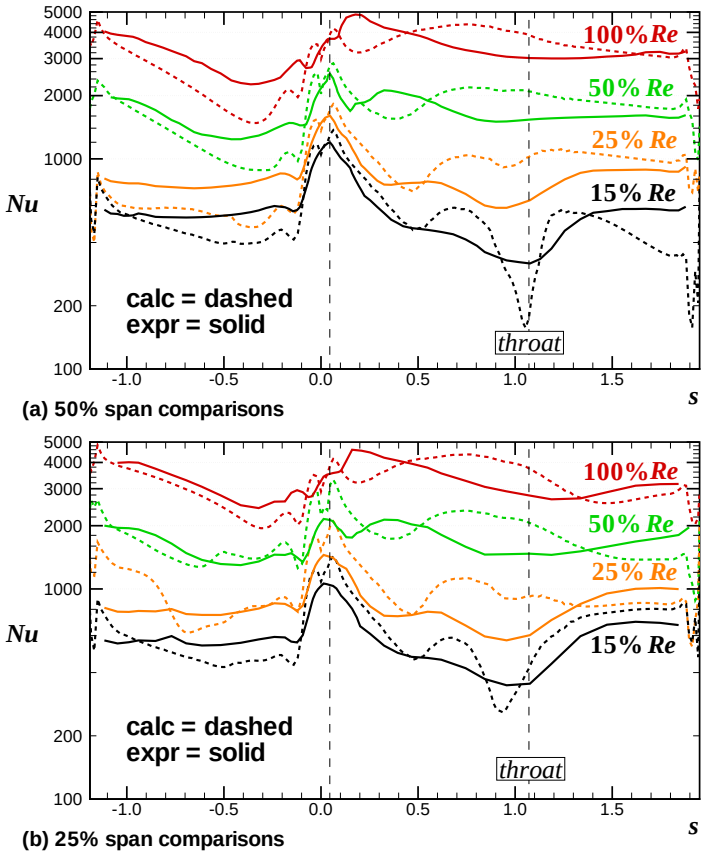

Figure 9. Effects of Reynolds Number on Heat Transfer

in Fig. 9 for variations in Reynolds number. Comparisons are made separately in the figure at 50% and 25% of span. Many of the comments made in the previous discussions are brought out here, particularly the pressure surface relaminarization effects for the 15% and 25% Re cases, the differences in the local peak heat transfer near $s \approx -0.1$, the stagnation point heat transfer, and the variations in suction surface transition location.

The data at the midspan stagnation points can be further analyzed by comparing the measured values to established data. Van Fossen et al. (1995) studied stagnation region heat transfer on isolated elliptical leading edges. They developed the following correlation for a stagnation point turbulent augmentation factor:

$$\frac{Fr_{Tu}}{Fr_{lam}} = 0.00851\sqrt{Tu\, Re_d^{0.8}\left(\frac{\Lambda_x}{d}\right)^{-0.574}} + 1.0 \qquad (2)$$

The leading edge of the blade corresponds to an ellipse with an aspect ratio of 1.5. Van Fossen et al. (1995) gave a laminar Frossling number of 0.870 for this aspect ratio. The stagnation point data of the current study is shown in Fig. 10 along with Eq. 2 with $Tu = 0.13$ and $\Lambda_x/d = 1.42$. Lines that are $\pm 4\%$ off of the correlation are also shown in the figure as was done in the original reference. Data from all cases obtained for this blade are shown in the figure, including some that are not described in detail in this report. Figure 10 shows that the agreement with the correlation is good. Only a slight decrease in inlet turbulence, or an increase in length scale would improve the agreement even more.

Effects of Pressure Ratio

The isentropic exit pressure ratio was varied from -25% to $+20\%$ of the nominal design value of 1.443. The exit Reynolds number was held at 50% of the design value for these measurements because facility limits prevented lower pressure ratios at the 100% Re condition (see Fig. 3). The independent inlet and exhaust control of the facility allowed the nominal exit Reynolds number to be held fixed while varying the cascade pressure ratio. Because of compress-

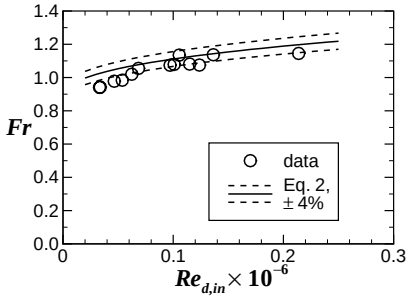

Figure 10. Stagnation Point Heat Transfer Data and Correlation

ibility effects, changes in the inlet Reynolds number were found to be small but not insignificant. Relative to the nominally fixed exit Reynolds number, Re_{in} changed +9.2% for a −25% change in PR and changed −4.9% for a +20% change in PR.

The results for Case 6 are shown in Fig. 11. Comparing this to Case 2 in Fig. 6 shows the effects of an exit isentropic pressure ratio increase of 20%. On the fully turbulent pressure surface, those effects are relatively minor and are representative of the 4% decreases that are expected from Re_{in} changes of −5%. Differences on the suction surface are more significant because of the effect that the lower inlet Reynolds number has on transition near the stagnation point. This effect is seen most clearly in the midspan data comparison shown in Fig. 12. Transition is moved back on the suction surface and heat transfer levels are lower on the remainder of the blade. The midspan data of Case 5 at −25% PR are also shown in Fig. 12. Here again, the Nusselt number differences on the fully turbulent pressure surface of ≈ +7% are consistent with the 9% increase in inlet Reynolds number. The suction surface transition start has moved correspondingly closer to the leading edge as expected. Note that the reduced pressure ratio has caused the peak heat transfer rate following transition to exceed that of the stagnation point. The midspan stagnation point data for all three of these cases are included in Fig. 10.

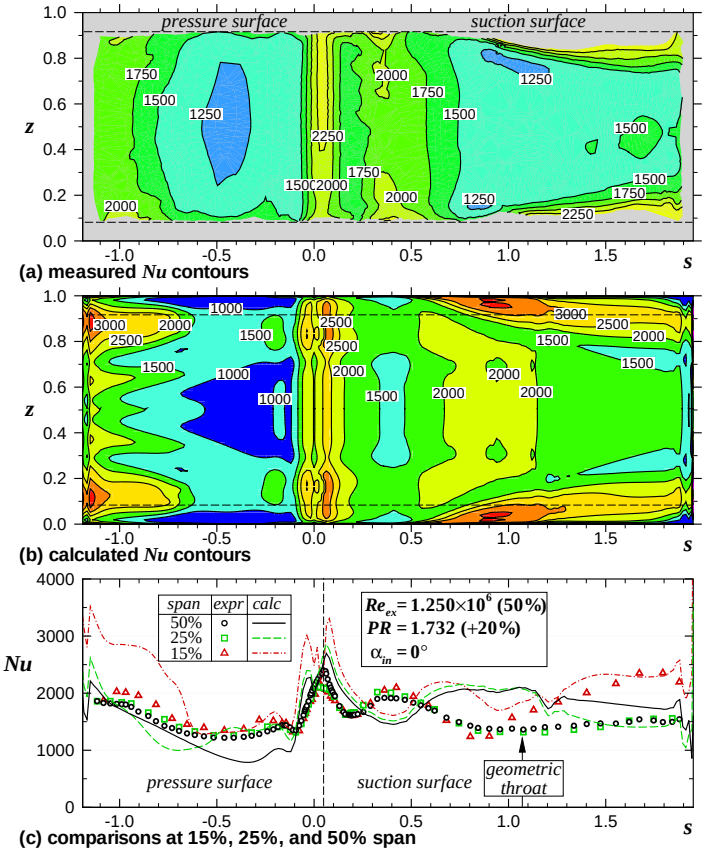

Figure 11. Heat Transfer Distributions - Case 6

Effects of Incidence Angle

The primary effects of incidence angle variation are two-dimensional in nature, so full-span contour plots will not be shown for these cases. Figure 13 compares the data obtained with +5 and −5 deg of incidence to those of design inlet flow angle, all at 50% of the nominal exit Reynolds number and at the nominal pressure ratio. In terms of surface distance, the total change in stagnation point location for inlet angle variations of ±5 deg is $\Delta s < 0.02$. The changes in heat transfer brought about by changes in inlet Reynolds number are again apparent. As seen in Table 1, relative changes in Re_{in} are significant; −7.7% for the −5 deg case and +17.2% for the +5 deg case. These changes affect the stagnation point heat transfer (also see Fig. 10). The pressure surface region just downstream of the stagnation region is affected directly by the change in inlet flow angle. Also on the pressure surface, the local heat transfer peak caused by the adverse pressure gradient region downstream of $s \approx -0.1$ is enhanced for the −5 deg case and almost eliminated for the +5 deg case. Near the pressure surface trailing edge, the measured Nu differences from the design data again tend to approach the differences expected for fully turbulent flow, i.e., about −6% for the −5 deg case and about +13% for the +5 deg case.

Differences in Nu on the suction surface again appear to be driven primarily by differences in Re_{in}. The higher inlet Reynolds number for the +5 deg case drives the transition location closer to the stagnation point while the lower inlet Reynolds number for the −5 deg case drives the transition location farther aft on the blade.

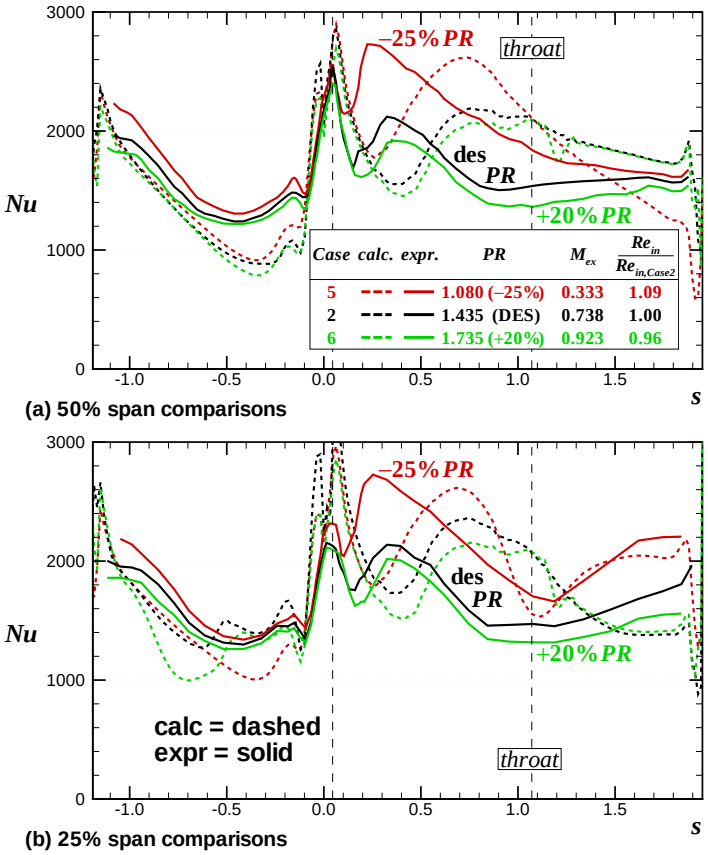

Figure 12. Effects of Pressure Ratio on Heat Transfer

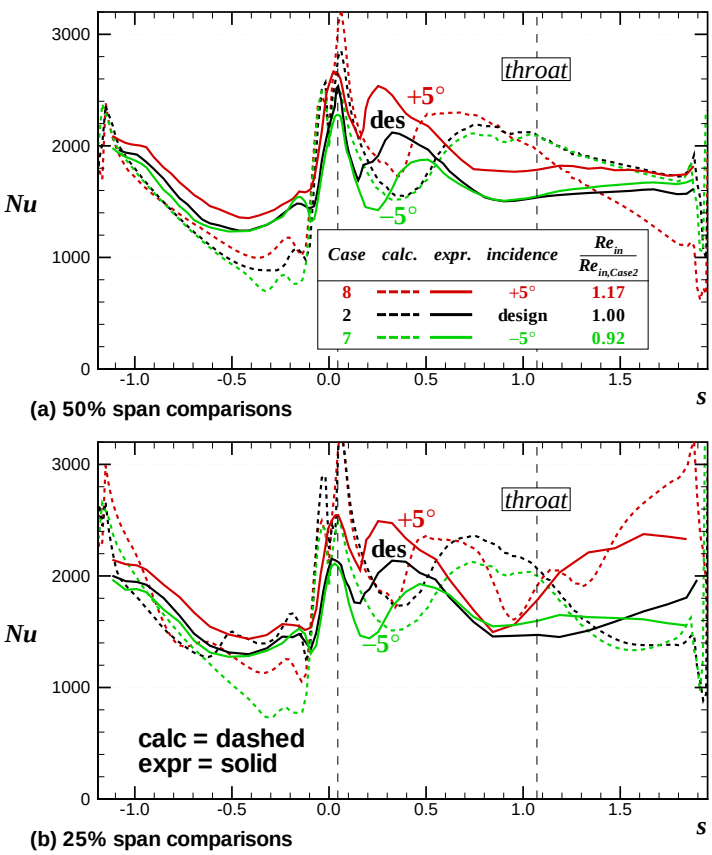

Figure 13. Effects of Inlet Flow Angle on Heat Transfer

COMPUTATIONAL HEAT TRANSFER RESULTS

The heat transfer predictions are discussed, first for the pressure surface, then for the leading edge region, and finally for the suction surface.

Pressure Surface

At the highest Reynolds number, Fig. 5 shows that pressure surface is turbulent almost everywhere. At mid and quarter span towards the rear of the pressure surface, data and analysis show higher Nusselt numbers than towards the rear of the suction surface. Figure 5(c) shows that the analysis agrees with the pressure surface data at 15% and 25% of span. At midspan the analysis underpredicts the pressure surface heat transfer. Since secondary flows near the blade pressure surface move towards the endwalls, the analysis appears to be overpredicting the pressure surface boundary layer thickness.

Figure 6 shows that the agreement with the data at 50% of design Reynolds number is somewhat better than the agreement shown in Fig. 5.

The data in Fig. 7 show a very flat pressure surface heat transfer distribution. This is characteristic of laminar flow. Figure 4(c) shows that relaminarization was predicted at this Reynolds number. At midspan the analysis is somewhat lower than the data. It would be considerably lower if augmentation due to freestream turbulence was neglected. At midspan Nu would be less than 340 over much of the pressure surface. The underprediction near $s = -0.3$ illustrates a difficulty with the augmentation model. Along the pressure surface the pressure gradient is first favorable, then adverse, and then favorable again. The velocity gradient augmentation model gives μ_t augmentation only for favorable pressure gradients. Calculations were done where d in the equation for μ_t was replaced by the surface distance. Agreement with data was not improved, and the shape of the Nusselt number distribution was no longer flat. Because μ_t increased with distance, the Nusselt number distribution was similar in shape to those seen in Figs. 5 and 6. At the other two spanwise locations shown in Fig. 7(c) the agreement is good for the forward half of the pressure surface and poor for the rear portion of this surface. The data in Fig. 7(a) show increased heat transfer near the rear corners

of the pressure surface. The analysis shows the same trend, but with a much higher increase in Nu. The reason for this behavior is not well understood. Here transition is not the cause of the high heat transfer. Relaminarization was predicted near $s = -0.5$ at mid and quarter span, although it was delayed until $s = -0.8$ near 15% of span. Variations in the relaminarization location would not account for the differences between mid and quarter span. They could be responsible for some of the differences between the 15% and 25% of span results. Augmentation due to freestream turbulence was not the cause of the high corner region heat transfer. Calculations done without augmentation showed similar heat transfer distributions.

Figure 8 shows that at the lowest Reynolds number, where K is well above the critical value, the pressure surface heat transfer is reasonably well predicted. Without augmentation, the predicted pressure surface heat transfer is less than 300 for $-0.8 < s < -0.45$.

Overall, while the augmentation model improves agreement with data, pressure surface heat transfer is underpredicted near adverse pressure gradient regions. But here the model is turned off. Figures 5 and 6 show good agreement when the pressure surface boundary layer is mostly turbulent.

Figures 12 and 13 show only small variations in experimental pressure surface heat transfer resulting from variations in either pressure ratio or flow angle. At midspan, the predicted variations are close to what is expected from the Reynolds number variations. At the -5 deg flow angle the adverse pressure gradient is reduced, and computationally, the laminar region is extended. At 25% of span the analysis agrees with the data at the design condition. At off-design conditions the analysis is more likely to underpredict the data.

Leading Edge Region

The leading edge region is the region between $-0.01 < s < 0.03$. The predictions often show a double peak in the stagnation region. The double peak is the result of using U_{fs} instead of U_{in} to calculate μ_t. Near stagnation U_{fs} is much less than U_{in}. Because of the double peak, line plots with closely spaced peaks are less able than contour plots to illustrate differences between measurements and predictions. The contour plots show a single color for a range of Nu values, (500 in Fig. 5). Peaks and valleys will be in different bands if they differ by more than the range. The peak predicted heat transfer is higher than the data. The degree of agreement between the analysis and data is similar for all cases in the leading edge region. Calculations done using just the Smith and Kuethe (1966) model gave leading edge region Nusselt numbers as high as the higher of the two peaks seen in the figures. This is not surprising in light of the results shown in Fig. 10, where the increase in the Frossling number is less than 30%. As discussed by Van Fossen et al. (1995), correlations which are independent of length scale give augmentations in excess of 50% for the conditions seen in this experiment. Dullenkopf and Mayle (1995) show that variations in the scale of turbulence can vary the turbulence augmentation by nearly a factor of three. These results indicate the necessity of including the scale of turbulence in models to predict the effects of turbulence on laminar heat transfer. Calculations with no augmentation due to turbulence underpredicted leading edge region almost as much as the Smith and Kuethe model for μ_t overpredicted the data.

Figures 9, 12, and 13 show that at midspan the analysis agrees reasonably well with the data. The predictions are somewhat higher, but not excessively so. At 25% of span the analysis shows higher heat transfer than at midspan. The data show no significant spanwise variation. The analysis shows even higher heat transfer close to the endwalls. This is not seen in the data. However, the unheated region on the blade close to the endwalls could account for the absence of high heat transfer near the endwall. Overall, the analysis is higher than the data in this region. Assuming that the model for predicting leading edge turbulence effects is accurate, leads to the conclusion that the analysis should have been done with a lower inlet turbulence intensity. Alternatively, a model accounting for turbulence scale, might have given improved data agreement.

Suction Surface

The data in Fig. 5(a) show high heat transfer just outside the leading edge region. Here, the highest heat transfer is seen at midspan. The midspan prediction shows a dip in the heat transfer, followed by a rise that exceeds the experimental data. This is followed by a decrease to the experimental values near the trailing edge. Transition is not complete in the analysis until $s \approx 0.4$. The resulting thin boundary layer gives higher heat transfer over much of the remaining part of the suction surface. The data are consistent with an abrupt suction surface heat transfer transition. Even though the measured arithmetic surface roughness of 6.5 μm is low, the Reynolds number is high. Boyle and Senyitko (2003) investigated the effects of surface roughness on loss. They and Pinson and Wang (2000) found that transition was initiated by low k^+ values. Boyle and Senyitko showed that the roughness transition length was short with respect to losses. They proposed a correlation to account for roughness transition, and a recommendation to determine the equivalent roughness height from the roughness measurement. Measurements indicated that

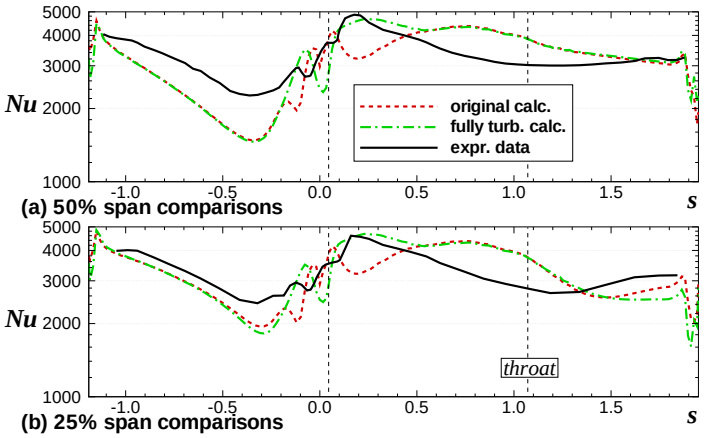

Figure 14. Comparison With Fully Turbulent Calculations - Case 1

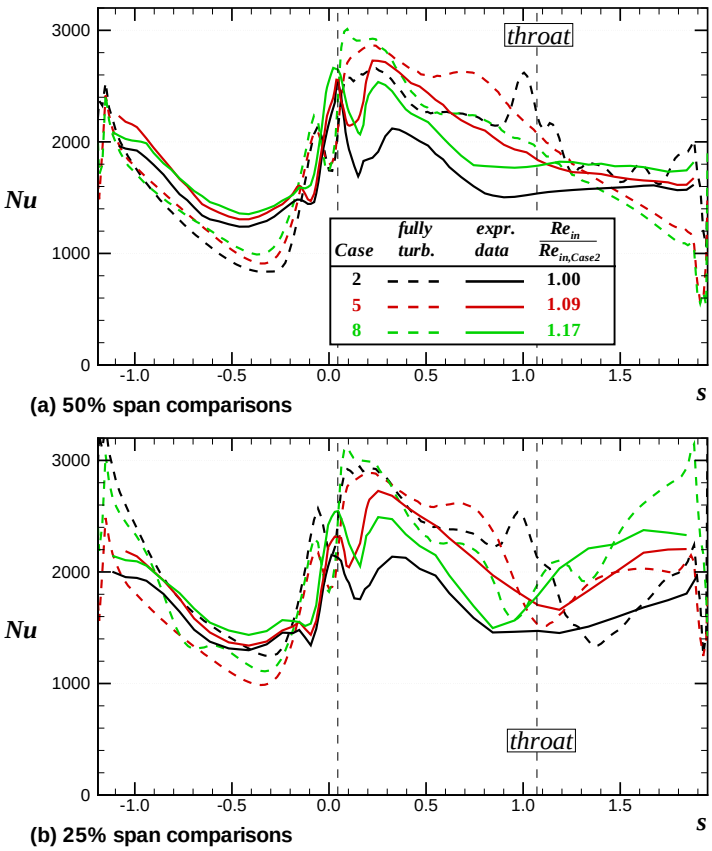

Figure 15. Comparison With Fully Turbulent Calculations - Cases 2, 5, and 8

the roughness transition could have occurred at the two highest Reynolds numbers. Transition would be fairly close to the leading edge, and much sooner than would be predicted using Mayle's smooth surface transition model. Although the roughness criterion was not incorporated into the three-dimensional heat transfer analysis, fully turbulent calculations were made. Figure 14 compares data and calculations using the fully turbulent assumption. At this high Reynolds number there are very little history effects, and the predicted heat transfer in the turbulent region does not change. For $0 < s < 0.4$ the fully turbulent assumption gives better data agreement.

Figure 5(c) shows good agreement between predictions and data at 15% of span. As Fig. 5(b) shows, this is a region of both high heat transfer rates, and high heat transfer gradients. This region, mostly downstream of the throat, sees upwash from endwall flows. The good agreement in this region validates the basic three-dimensional Navier-Stokes approach. The flows are turbulent, so that modeling issues associated with transition and buffeted laminar flows do not influence the results.

Table 1 shows that, at $Re_{ex} = 1.2 \times 10^6$, there are a range of inlet Reynolds numbers. The 17% increase in Re_{in} between Cases 2 and 8 represents about the same percentage increase in k^+. Figure 15 compares data and fully turbulent predictions for Cases 2, 5, and 8. At the highest Re_{in} shown in Fig. 15 an assumption of fully turbulent flow is appropriate. But, reducing the Reynolds number by 17% shows the smooth surface transition prediction to be more appropriate. As the Reynolds number, and thus k^+, is decreased, smooth surface transition is more appropriate.

Interestingly, the results in Fig. 7 at 25% of the design Reynolds number imply that the start of transition occurred prematurely in the prediction. However, the augmentation model also influences the results. Without augmentation a minimum Nu of 600 is reached near $s = 0.35$, and rises to 1000 near $s = 1$. Transition occurred for $0.35 < s < 1.0$. Augmentation decreased linearly with increased intermittency. But here a linear relationship was not appropriate. Figures 8(b) and 8(c) show accurate heat transfer predictions at the lowest Reynolds number. Here the behavior in the transition region is well predicted. The midspan predicted heat transfer over the last third of the suction surface is lower than the data. But, by 25% of span, the analysis slightly overpredicted the suction surface heat transfer.

For all Reynolds numbers the predicted and measured full span heat transfer show high Nu values near the endwalls for the rear half of the suction surface. In this region the agreement with data is very good.

Figures 14 and 15 show that, after the likelihood of tripping the boundary layer at the higher Reynolds numbers is accounted for, the analysis is in reasonably good agreement with the data. The change in heat transfer with changes in flow conditions is well predicted. Figure 13(b) shows a large increase in quarter span suction surface heat transfer

at the higher inlet flow angle. This behavior is predicted by the analysis.

SUMMARY AND CONCLUSIONS

Detailed aerodynamic and heat transfer measurements and predictions were given for a power generation turbine rotor under engine specific conditions. The effects of variations in Reynolds number, exit pressure ratio, and incidence angle were quantified. The primary effect of Reynolds number variations in the range of 15% to 100% of the design value was to move the location of the laminar-to-turbulent transition on the suction surface and to drive relaminarization on the pressure surface at the lower Reynolds numbers. Variations in isentropic exit pressure ratio over a range of -25% to $+20\%$ were found to have little direct effect on the blade heat transfer, but an indirect effect was seen through the differences in inlet Reynolds number. Inlet flow angle variations of of ± 5 deg affected a small adverse pressure gradient region downstream of the stagnation point and also affected the inlet Reynolds number which had an impact on the suction surface transition location. The data appeared to agree well with appropriate scaling laws and showed good agreement with a stagnation point heat transfer correlation.

The good spatial resolution due to the large scale and the liquid crystal measurement technique allowed the secondary flow effects to be clearly quantified. These secondary flows significantly increased suction surface heat transfer rates near the endwalls. The data also quantified the three-dimensional impact of laminar-to-turbulent transition on blade heat transfer. Good midspan symmetry was observed for all cases.

A goal of a CFD heat transfer prediction is to predict the data to within the uncertainty of the measurements. While these predictions showed most of the trends in the data, this goal was not met. At the two highest Reynolds numbers, suction surface transition start and length were not accurately predicted. Roughness measurements indicated that roughness could have caused the abrupt transition. Roughness should be considered in predicting heat transfer, especially at high Reynolds numbers. At the two lowest Reynolds numbers, suction surface transition was reasonably well predicted. The approach used to predict the effects of turbulence on laminar heat transfer tended to overpredict the heat transfer in the leading edge region and and to underpredict it on the pressure surface. Most likely this resulted from not including a turbulence scale effect in the augmentation modeling. Near midspan the analysis underpredicted the pressure surface heat transfer. Away from midspan the analysis was more likely to overpredict the heat transfer.

ACKNOWLEDGMENT

This work was conducted under Space Act Agreement FA-147 between NASA and the General Electric Corporation. It was supported by the NASA Glenn Research Center under contract NAS3-00145 with QSS Group, Inc. The assistance of Mr. Kevin Radil of the U.S. Army Vehicle Propulsion Directorate in measuring the surface roughness is gratefully acknowledged as is the support of Mr. Jason Morey of Syracuse University in digitizing the heat transfer data.

REFERENCES

Ames, F. E., and Moffat, R. J., 1990, "Heat Transfer with High Intensity, Large Scale Turbulence: The Flat Plate Turbulent Boundary Layer and the Cylindrical Stagnation Point," Dept. of Mech. Eng. Report No. HMT-44, Stanford Univ., Stanford CA.

Arnone, A, Liou, M.-S, and Povinelli, L. A., 1992, "Navier- Stokes Solution of Transonic Cascade Flows Using Non-Periodic C-Type Grids," AIAA *Journal of Propulsion and Power,* Vol. 8, No. 2, pp. 410–417.

Arts, T., Duboue, J.-M., and Rollin, G., 1998, "Aerothermal Performance Measurements and Analysis of a Two-Dimensional High Turning Rotor Blade," ASME *Journal of Turbomachinery,* Vol. 120, No. 3, pp. 494–499.

Baughn, J. W., Butler, R. J., Byerley, A. R., and Rivir, R. B., 1995, "An Experimental Investigation of Heat Transfer, Transition and Separation on Turbine Blades at Low Reynolds Number and High Turbulence Intensity," ASME paper 95-WA/HT-25.

Blair, M. F., 1994, "An Experimental Study of Heat Transfer in a Large-Scale Turbine Rotor Passage," ASME *Journal of Turbomachinery,* Vol. 116, No. 1, pp. 1–13.

Boyle, R. J., and Giel, P. W., 1995, "Three-Dimensional Navier-Stokes Heat Transfer Predictions for Turbine Blade Rows," AIAA *Journal of Propulsion and Power,* Vol. 11, No. 6, pp. 1179–1186.

Boyle, R. J., and Simon, F. F., 1999, "Mach Number Effects on Turbine Blade Transition Length Prediction," ASME *Journal of Turbomachinery,* Vol. 121, No. 4, pp. 694–702.

Boyle, R. J., Lucci, B. L., and Senyitko, R. G., 2002, "Aerodynamic Performance and Turbulence Measurements in a Turbine Vane Cascade," ASME paper GT-2002-30434.

Boyle, R. J., and Senyitko, R. G., 2003, "Measurements and Predictions of Surface Roughness Effects on Turbine Vane Aerodynamics," to be presented at the ASME Turbo Expo as paper GT-2003-38580.

Camci, C. and Arts, T., 1991, "Effect of Incidence on Wall Heating Rates and Aerodynamics on a Film Cooled Transonic Turbine Blade," ASME *Journal of Turbomachinery,* Vol. 113, No. 3, pp. 493–513.

Chima, R. V., and Yokota, J. W., 1990, "Numerical Analysis of Three-Dimensional Viscous Internal Flows," AIAA *Journal*, Vol. 28, No. 5, pp. 798–806.

Chima, R. V., 1991, "Viscous Three-Dimensional Calculations of Transonic Fan Performance," AGARD Propulsion and Energetics Symposium on Computational Fluid Mechanics for Propulsion, San Antonio, Texas, May 27–31.

Chima, R. V., Giel, P. W., and Boyle, R. J., 1993, "An Algebraic Turbulence Model for Three-Dimensional Viscous Flows," AIAA paper 93-0083, (NASA TM-105931).

Dullenkopf, K., and Mayle, R. E., 1995, "An Account of Free-Stream-Turbulence Length Scale on Laminar Heat Transfer," ASME *Journal of Turbomachinery*, Vol. 117, pp. 401–406.

Dunn, M. G., Kim, J., Civinskas, K. C., and Boyle, R. J., 1994, "Time-Averaged Heat Transfer and Pressure Measurements and Comparison with Predictions for a Two-Stage Turbine," ASME *Journal of Turbomachinery*, Vol. 116, pp. 14–23.

Giel, P. W., Thurman, D. R., Lopez, I., Boyle, R. J., Van Fossen, G. J., Jett, T. J., Camperchioli, W. P., and La, H., 1996, "Three-Dimensional Flow Field Measurements in a Transonic Turbine Cascade," ASME paper 96-GT-113.

Giel, P. W., Van Fossen, G. J., Boyle, R. J., Thurman, D. R., and Civinskas, K. C., 1999, "Blade Heat Transfer Measurements and Predictions in a Transonic Turbine Cascade," ASME paper 99-GT-125.

Giel, P. W., Bunker, R. S., Van Fossen, G. J., and Boyle, R. J., 2000, "Heat Transfer Measurements and Predictions on a Power Generation Gas Turbine Blade," ASME paper 2000-GT-0209.

Graziani, R. A., Blair, M. F., Taylor, R. J., and Mayle, R. E., 1980, "An Experimental Study of Endwall and Airfoil Surface Heat Transfer in a Large Scale Turbine Blade Cascade," ASME *Journal of Engineering for Power,* Vol. 102, No. 2, pp. 1–11.

Guenette, G. R., Epstein, A. H., Giles, M. B., Haimes, R., and Norton, R. J. G., 1989, "Fully Scaled Transonic Turbine Rotor Heat Transfer Measurements," ASME *Journal of Turbomachinery,* Vol. 111, No. 1, pp. 1–7.

Joslyn, D., and Dring, R., 1992, "Three-Dimensional Flow in an Axial Turbine: Part 1 — Aerodynamic Mechanisms," ASME *Journal of Turbomachinery,* Vol. 114, No. 1, pp. 61–70.

Kline, S. J., and McClintock, F. A., 1953, "Describing Uncertainty in Single-Sample Experiments," *Mechanical Engineering,* Vol. 75, Jan., pp. 3–8.

Langston, L. S., 1980, "Crossflows in a Turbine Cascade Passage," ASME *Journal of Engineering for Power,* Vol. 102, pp. 866–874.

Mayle, R. E., 1991, "The Role of Laminar-Turbulent Transition in Gas Turbine Engines," ASME *Journal of Turbomachinery,* Vol. 113, pp. 509–537.

Moffat, R. J., 1990, "Experimental Heat Transfer," *Proc. of the Ninth Int'l Heat Transfer Conf.,* Jerusalem, Israel, Vol. 1, pp. 187–205.

Pinson, M. W., and Wang, T., 2000, "Effect of Two-Scale Roughness on Boundary Layer Transition over a Heated Flat Plate: Part 1 - Surface Heat Transfer," ASME *Journal of Turbomachinery,* Vol. 122, pp. 301–307.

Schlichting, H., 1979, *Boundary-Layer Theory*, Seventh Edition, McGraw-Hill, New York, p. 714.

Smith, M. C. and Kuethe, A. M., 1966, "Effects of Turbulence on Laminar Skin Friction and Heat Transfer," *The Physics of Fluids,* Vol. 9, No. 12, pp. 2337–2344.

Solomon, W. J., Walker, G. J., and Gostelow, J. P., 1995, "Transition Length Prediction For Flows With Rapidly Changing Pressure Gradients," ASME paper 95-GT-241.

Steelant, J., and Dick, E., 1999, "Prediction of By-Pass Transition by Means of a Turbulence Weighing Factor - Part 1: Theory and Validation," ASME paper 99-GT-29.

Thulin, R. D., Howe, D. C., and Singer, I. D., 1982, "Energy Efficient Engine – High-Pressure Turbine Detailed Design Report," NASA CR-165608.

Van Fossen, G. J., Simoneau, R. J., and Ching, C. Y., 1995, "Influence of Turbulence Parameters, Reynolds Number, and Body Shape on Stagnation-Region Heat Transfer," ASME *Journal of Heat Transfer,* Vol. 117, pp. 597–603, also NASA TP 3487, 1994.